

Effects of synthesis parameters on the properties and photocatalytic activity of the magnetic catalyst TiO₂/CoFe₂O₄ applied to selenium photoreduction

Original

Effects of synthesis parameters on the properties and photocatalytic activity of the magnetic catalyst TiO₂/CoFe₂O₄ applied to selenium photoreduction / Fuziki, M. E. K.; Brackmann, R.; Dias, D. T.; Tusset, A. M.; Specchia, S.; Lenzi, G. G.. - In: JOURNAL OF WATER PROCESS ENGINEERING. - ISSN 2214-7144. - STAMPA. - 42:102163(2021).
[10.1016/j.jwpe.2021.102163]

Availability:

This version is available at: 11583/2905978 since: 2021-06-10T18:52:42Z

Publisher:

Elsevier B.V.

Published

DOI:10.1016/j.jwpe.2021.102163

Terms of use:

This article is made available under terms and conditions as specified in the corresponding bibliographic description in the repository

Publisher copyright

(Article begins on next page)

Article: EFFECTS OF SYNTHESIS PARAMETERS ON THE PROPERTIES AND PHOTOCATALYTIC ACTIVITY OF THE MAGNETIC CATALYST $\text{TiO}_2/\text{CoFe}_2\text{O}_4$ APPLIED TO SELENIUM PHOTOREDUCTION

Authors: M. E. K. Fuziki^{1,2 †}, R. Brackmann³, D. T. Dias⁴, A. M. Tusset⁵, S. Specchia⁶, G. G. Lenzi¹

¹Departamento de Engenharia Química, Universidade Tecnológica Federal do Paraná, Rua Doutor Washington Subtil Chueire, 330, Ponta Grossa, PR 84017-220, Brazil.

²Departamento de Engenharia Química, Universidade Estadual de Maringá, Avenida Colombo, 5790, Maringá, PR 87020-900, Brazil.

³Departamento de Química, Universidade Tecnológica Federal do Paraná, Via do Conhecimento, s/n—Km 01, Pato Branco, PR 85503-390, Brazil.

⁴Departamento Acadêmico de Física, Universidade Tecnológica Federal do Paraná, Rua Doutor Washington Subtil Chueire, 330, Ponta Grossa, PR 84017-220, Brazil.

⁵ Departamento Acadêmico de Matemática, Universidade Tecnológica Federal do Paraná, Rua Doutor Washington Subtil Chueire, 330, Ponta Grossa, PR 84017-220, Brazil.

⁶Department of Applied Science and Technology, Corso Duca degli Abruzzi 24, Torino 10129, Italy

[†] Corresponding author.

E-mail address: mariafuziki@alunos.utfpr.edu.br (M. E. K. Fuziki)

Abstract

Selenium contamination in water bodies is a concerning issue due to the harmful effects of the excessive selenium intake to human health. Heterogeneous photocatalysis can be successfully applied in selenium reduction, but the photocatalyst recovery in the end of the process still needs improvement. The present work investigated the application of magnetic photocatalysts ($\text{TiO}_2/\text{CoFe}_2\text{O}_4$) in the Se(IV) photoreduction. The sol-gel method was used in the photocatalyst synthesis, and a central composite design was considered to guide the experiments. The effects of titanium isopropoxide mass ratio used in the synthesis, calcination temperature and pH on Se(IV) reduction were evaluated. The results indicated a strong influence of the calcination temperature and solution pH values closer to 3.5 showed the best removal results. In the optimum conditions, it was possible to promote more than 99% selenium removal after 2 min of exposure to radiation. The rutile phase presence in the photocatalysts presented a negative impact in the removal efficiency. In addition, the synthesized photocatalysts were magnetically recoverable, which favored the catalyst recovery and reuse in the photoreduction of Se(IV).

Keywords: Photocatalysis; Experimental Design; Heavy Metal; Magnetic Photocatalyst

1. INTRODUCTION

Selenium (Se) is a trace element naturally found in rocks, soil and foods [1–3], whose intake in small amounts is essential for living organisms [3,4]. Large amounts of Se in the diet, however, can be harmful. In rodents, for example, both excessive or deficient Se intake can affect the normal hair growth [5] and the sperm quality [6] of these animals. In humans, chronic Se intoxication (selenosis) has nail and hair loss, fatigue, irritation, and nervous problems as main symptoms [3]. Some studies conducted with a group of residents of a city in northern Italy suggest that long-term consumption of water containing high Se(VI) levels may be related to the increased incidence of certain types of cancer and neurodegenerative diseases [7–9]. Also, spinal and craniofacial deformities observed in young fish of a lake (Kentucky) were attributed to the high Se concentration in these animals tissues (on average, 7.1 mg kg⁻¹) [10]. In aqueous solution, Se is most commonly found as inorganic anions – selenide (Se²⁻), selenite (SeO₃²⁻) and selenate (SeO₄²⁻) [11–13] – which are considered to be more toxic than organic Se forms, such as selenomethionine [3]. Besides, Se contamination in aquatic environments is even more alarming because of its bioaccumulation capacity in the food chain [2].

Thus, there is a concern about controlling selenium intake, which for an adult should not exceed the maximum daily limit of 400 µg [14]. Also in this sense, the Brazilian Ministry of Health established a maximum permitted selenium concentration of 0.01 mg L⁻¹ in water as the potability standard [15]. Unfortunately, certain human activities, such as mining, agriculture and the burning of fossil fuels (such as coal) have been affecting the natural cycle of selenium, leading to an increase in its concentration in certain areas [2,16]. There are, for example, reports of Se concentration increase in soil and water in regions close to coal-fired power plants [10,17].

According to the World Health Organization, selenium concentration in water must not exceed 40 µg L⁻¹ [18]. Given the harmful effects of selenium pollution, different physical, chemical and biological techniques have been applied to Se removal from water [1,19]. These techniques, however, present some limitations: biological processes, for example, are limited by the inhibitory effect of formed elemental Se, chemical techniques normally depend on high-cost reagents, while physical methodologies, like adsorption, can only concentrate selenium ions [13]. Thus, heterogeneous photocatalysis stands out for overcoming these limitations, allowing the recovery and reuse of the catalyst and for being a photochemical process that can be carried out under sunlight [20–23].

Heterogeneous photocatalysis consists of the application of a photocatalyst (semiconductor), which, by absorbing photons with energy equal or greater than its band-gap, produces electrons/holes (e⁻/h⁺) pairs capable of promoting redox reactions of substances adsorbed on the photocatalyst surface [21,24]. This process has already been proved capable of reducing the Se (IV) and Se (VI) forms to

elemental selenium, thus removing Se from the aqueous medium [13]. Studies conducted in this regard have indicated that the process can be carried out using titanium dioxide as a photocatalyst, under acidic pH conditions and with the addition of formic acid [25]. The existing literature, however, is limited to the application of TiO₂-based photocatalysts in the form of fine suspended particles [13,25–30]. Thus, there is still much to explore about the type of photocatalyst used in Se reduction, especially with regard to the catalyst separation improvement. Photocatalysts are normally used in suspension, which guarantees a large surface area available for reactions, in addition to reducing limitations of mass and photon transfer presented by immobilized catalysts [31]. However, the use of suspended catalysts entails costs and time spent in post-treatment catalyst separation [32]. Recently, the use of catalysts with magnetic cores is gaining attention since they combine the large surface area of suspended catalysts and the ease of magnetic separation [33–35].

In this context, in the present work, magnetic photocatalysts, TiO₂/CoFe₂O₄, were synthesized by the combination of sol-gel methodologies and applied to selenium photoreduction. The study focused on the evaluation of the effects of the synthesis parameters on the photocatalytic properties and activity of the catalyst. The considered effects were titanium isopropoxide/CoFe₂O₄ mass ratio and calcination temperature used on the synthesis, and also pH used during photocatalysis as an operational condition. Both the synthesis process and the photocatalytic tests were guided by a central composite design (CCD). The use of an experimental design methodology is justified since it provides greater efficiency in the acquisition of information about the process and reduction of time and costs associated with the realization of tests [36,37].

2. MATERIALS AND METHODS

2.1. Synthesis of the photocatalysts

The TiO₂/CoFe₂O₄ photocatalysts were synthesized in two consecutive stages: (I) magnetic material (CoFe₂O₄) preparation, followed by the (II) magnetic particles coating with a TiO₂ layer. The reagents used in the catalyst synthesis were cobalt nitrate (Co(NO₃)₂·6H₂O, 98% Synth), iron nitrate (Fe(NO₃)₃·9H₂O, 98% Synth), anhydrous citric acid (99.5%, Perquim), monoethylene glycol (99.5%, Dinâmica), titanium (IV) isopropoxide (TIPO, 97%, Aldrich) and absolute ethanol (≥99.9, Honeywell).

Cobalt ferrite (CoFe₂O₄) was synthesized using the Pechini method [38], with minor adaptations. An aqueous solution containing Co(NO₃)₂·6H₂O and Fe(NO₃)₃·9H₂O, in a molar ratio of 1:2 (Co:Fe), was mixed with citric acid (CA) aqueous solution, in a molar ratio of 3:1 (CA:M, with M representing the metal ions in the solution). Under magnetic stirring, the mixture temperature was

raised to 60 °C and kept constant for 30 min. Ethylene glycol (EG) was then added to the solution, in a mass ratio of 40:60 (EG:CA). The mixture temperature was raised to 85°C and maintained constant until the formation of a dark, reddish polymeric resin. This whole process took place inside a laboratory fume hood. The resin was then transferred to a crucible and calcined at 400°C during 5h, with a heating rate of 1 °C min⁻¹. Finally, the calcined material (CoFe₂O₄) was crushed and stored for later coating step.

In the next step, the obtained cobalt ferrite particles were covered with a TiO₂ layer, using a sol-gel process adapted from the work of Li et al. [39]. About 100 mg of the magnetic material (CoFe₂O₄) were dispersed in 40 mL of a titanium isopropoxide and ethanol solution. Different titanium isopropoxide/CoFe₂O₄ ratios (m/m) were obtained by varying the amount of titanium isopropoxide in ethanol between 5 and 20% (v/v) (see experimental design section in Supplementary Material, Table S1). The suspension was sonicated for 8 minutes, after which 12 mL of an ethanol/ultrapure water mixture (5:1, v/v) were added dropwise to the suspension, kept under vigorous magnetic stirring. The suspension remained under agitation for 12 h, at 25 °C and 200 rpm. The precipitate was magnetically separated, using a neodymium magnet (N35, neodymium-iron-boron alloy, dimensions 40mm x 40mm x 30mm, with an approximate 0.5 Tesla magnetic field at 5mm, with a force capable of lifting 69kg of iron), dried and calcined at a given temperature (T_{calc} , °C), for 5 h. The heating rate was 1 °C min⁻¹; every 100 °C interval, the temperature was kept constant for 30 min.

2.2. Experimental Design

The TiO₂/CoFe₂O₄ catalysts were synthesized by using different titanium isopropoxide/cobalt ferrite mass ratios (TIPO/CoFe₂O₄, m/m), during the coating step, and different calcination temperatures (T_{calc} , °C), during the thermal treatment step. The variation in these parameters followed two distinct central composite designs (CCDs). The first experimental design (CCD1) evaluated the effects of the two factors mentioned above (TIPO/CoFe₂O₄ mass ratio and T_{calc}) on the properties of the photocatalysts, determined by different characterization methods. The second experimental design (CCD2) was applied in order to evaluate the performance of catalysts in the photoreduction of Se(IV), considering the effects of three factors: the pH of the medium, TIPO/CoFe₂O₄ mass ratio and T_{calc} . Table 1 and Table 2 describe the variables and levels for CCD1 and CCD2, respectively.

Table 1 - Factors and Levels of the Two-Factor Central Composite Design (CCD1)

| Variables (Factors) | Levels | | | | |
|---|-----------|------|------|------|-----------|
| | $-\alpha$ | -1 | 0 | 1 | $+\alpha$ |
| x_1 : T_{calc} (°C) | 300 | 359 | 500 | 641 | 700 |
| x_2 : TIPO/CoFe ₂ O ₄ , (m/m) | 19.2 | 27.8 | 48.0 | 68.2 | 76.8 |

It was necessary to use two different experimental designs due to the difference between the α -values in a two-factor CCD (CCD1, $\alpha = 1.44$) and in a three-factor CCD (CCD2, $\alpha = 1.68$). To make the analysis more efficient, reducing the number of experiments and, at the same time, ensuring that the results of the two CCDs covered the same range of conditions for the synthesis of the catalysts, the two CCDs were designed so that levels (0), $(-\alpha)$ and $(+\alpha)$ of variables TIPO/CoFe₂O₄ mass ratio and T_{calc} coincided (See Supplementary material, Figure S1). The difference between them, therefore, is restricted to levels (-1) and $(+1)$. A second-order model was adjusted to the results obtained from the experimental designs, in order to build a response surface.

Table 2 - Factors and Levels of the Three Factors Central Composite Design (CCD2)

| Variables (Factors) | Levels | | | | |
|---|-----------|------|------|------|-----------|
| | $-\alpha$ | -1 | 0 | 1 | $+\alpha$ |
| x_1 : T_{calc} (°C) | 300 | 381 | 500 | 619 | 700 |
| x_2 : TIPO/CoFe ₂ O ₄ , (m/m) | 19.2 | 30.7 | 48.0 | 65.3 | 76.8 |
| x_3 : pH | 2.0 | 2.61 | 3.5 | 4.39 | 5.0 |

2.3. Catalysts characterization

The catalysts synthesized according to CCD1 had their structure characterized by X-ray diffraction (XRD) analysis, (MiniFlex 600, with Cu K α radiation, $\lambda = 1.5406 \text{ \AA}$) operated at 40 kV and 15 mA. The Scherrer equation (Eq. 1) was used to estimate the average crystallite sizes for anatase, rutile and cobalt ferrite phases. In Equation 1, d_m is the average crystallite size, k is a dimensionless constant (Scherrer constant), which depends on the shape of the crystallite (assumed 0.893), λ is the wavelength of incident radiation, in nanometers, θ is the diffraction angle in radians and L is the full width at half maximum (FWHM) of the peak, given in radians [40,41].

$$d_m = \frac{k \cdot \lambda}{\cos(\theta) \cdot L} \quad (1)$$

Anatase and rutile phase percentages present in the TiO₂/CoFe₂O₄ photocatalysts were determined using the Spurr and Myers Equation (Equation 2), in which f_A corresponds to the fraction of anatase in the sample, while I_A and I_R are, respectively, the intensities of the diffraction peaks (101) of anatase and (110) of rutile [41,42].

$$f_A = \frac{1}{\left(1 + 1,265 \frac{I_R}{I_A}\right)} \quad (2)$$

Besides, CCD1 catalysts had their surface evaluated by scanning electron microscopy (SEM) and energy-dispersive X-ray spectroscopy (EDS) (Tescan Scanning Electron Microscope, Vega 3 LMU equipped with dispersive energy detector –EDS- Oxford, AZTec Energy X-Act).

The N₂ adsorption/desorption method was used, in association with the model proposed by Brunauer, Emmet and Teller (BET), to determine the specific surface area of the materials. The point of zero charge (PZC) of the catalysts was obtained by using a batch equilibration method [43,44], described in more detail in the Supplementary Material.

Furthermore, photoacoustic spectroscopy (PAS) analyzes were performed in the ultraviolet–visible (UV-Vis) spectral regions with equipment consisting of: xenon arc lamp at 1000 W (66926, Newport Corporation/Oriel) as the light source; monochromator (74100, Newport Corporation / Oriel); mechanical modulator (SR540, Stanford Research Systems); lock-in amplifier (SR830, Stanford Research System); and standard photoacoustic cell (aluminum, 10 mm in diameter and 1.5 mm in thickness) with transparent quartz window (6 mm in diameter and 2 mm in thickness) and capacitive microphone (4953, Brüel & Kjaer, 12 mm in diameter, a gain of 50 mV Pa⁻¹, frequency response between 3 and 10 kHz, positioned at 15 mm from the chamber). All photoacoustic spectra were obtained at 23 Hz and recorded between 225 and 700 nm. The data were acquired using a personal computer, and the PAS spectra were normalized with respect to the carbon black signal. The photoacoustic spectra in the UV-VIS region obtained were used to find the direct band gap energy by the intersection of the line given by Equation (3), with the x-axis of the plot.

In Eq. 3, E_g is the band-gap energy, $h\nu$ is the photon energy and A is the absorption coefficient.

$$(a(h\nu))^2 = A(h\nu - E_g), \quad (3)$$

2.4. Photocatalytic tests

In each photocatalytic test, 250 mL of selenium solution (500 µg L⁻¹ of Se (IV) + 50 µL of formic acid, 85%) and 0.0250 g (0.1 g L⁻¹) of photocatalyst were used. The pH of the solution was adjusted between 2 and 5, according to the experimental design (CCD2), using HCl and NaOH solutions. After photocatalyst addition, the suspension was kept in the dark during 30 min, to achieve the adsorption equilibrium. The lamp was then turned on and, over the time of exposure to radiation (40 min), samples were collected, filtered using syringe filters (0.22 µm pores), diluted in 10% HCl solution, to adjust their concentration to the calibration curve, and stored for selenium concentration measurements by atomic absorption spectrophotometry with hydride generation (HG-AAS). To

estimate the error, the five replicates of the CCD2 central point were considered, with 95% confidence in the Student's t-test.

The photocatalysis experiments were carried out in a photocatalytic chamber with a metallic body, equipped with a mercury vapor lamp (250 W) positioned above a 600 mL glass reactor. The temperature of the solution was controlled using an ultra-thermostatic bath ($T_{\text{water}} = 20\text{ }^{\circ}\text{C}$) and a magnetic stirrer was employed to ensure vigorous and constant mixing.

Adsorption and photolysis tests were also carried out to verify the contribution of these processes in the Se(IV) removal. The experimental conditions were similar to those previously described, with the difference that, in the adsorption test, the suspension was kept in the dark (without radiation), while in the photolysis test, there was no addition of a catalyst to the solution.

Finally, a reuse test was performed. Five photocatalysis cycles (of 10 min each) were carried out in the same conditions of the CCD2 test with the best results. At the end of each cycle, a certain amount of Se(IV) standard solution and formic acid were added to the suspension, considering the reduction of the reaction volume caused by the sample collection, to reestablish the initial concentration of selenite for the start of a new cycle. Between cycles, no adsorption step was performed.

3. RESULTS

3.1. Characterization results

The CCD1 led to synthesis of nine $\text{TiO}_2/\text{CoFe}_2\text{O}_4$ photocatalysts (Figure 1a), whose visual aspect were quite different from the pure cobalt ferrite (Figure 1b) and the pure titanium dioxide (Figure 1c) samples. The synthesis parameters have affected the catalysts characteristics, like color and phase compositions, as summarized in the Figure 1a.

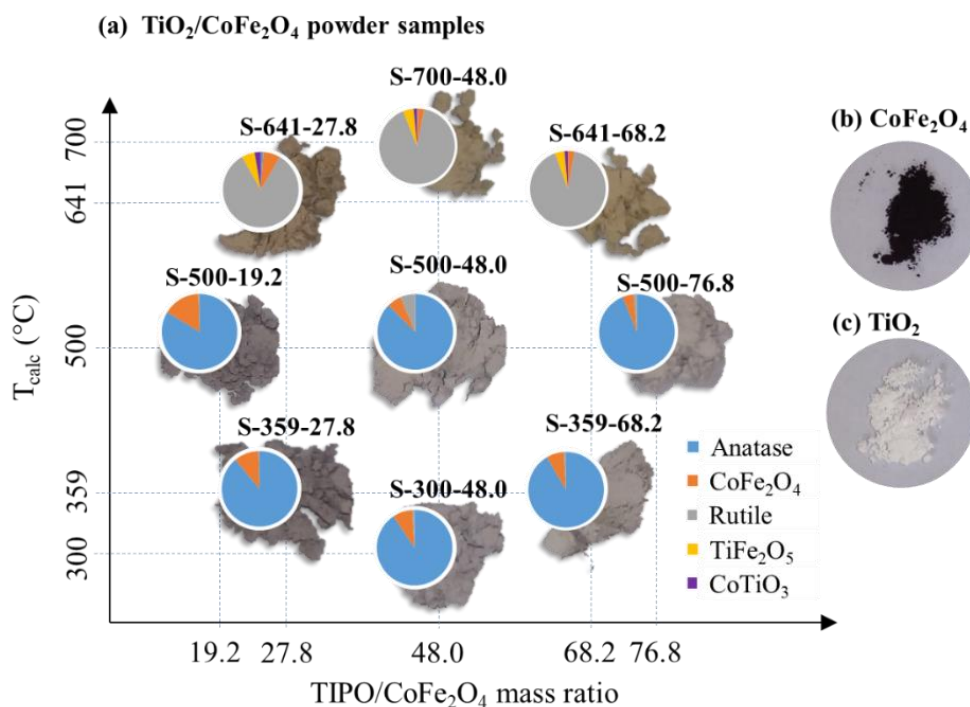


Figure 1 - (a) Diagram showing the nine catalysts synthesized following the CCD1 and their phase composition according to the Rietveld refinement results, (b) pure cobalt ferrite and (c) pure TiO_2 samples.

The main properties of the CCD1 catalysts (specific surface area, PZC and band gap) are summarized in Table 3. The characterization results of the photocatalysts are discussed in more detail in the following sections.

Table 3 - Specific surface area, point of zero charge (PZC) and band gap values for $\text{TiO}_2/\text{CoFe}_2\text{O}_4$ catalysts (CCD1)

| Catalyst | Specific surface area (BET, $\text{m}^2 \text{g}^{-1}$) | PCZ | Eg (eV) – Linear method |
|------------------------|--|------|----------------------------|
| S-359-27.8 | 78 | 6.78 | 2.99 |
| S-641-27.8 | 14 | 7.41 | 2.43; 3.06; e 3.47 |
| S-359-68.2 | 119 | 6.75 | 3.10 |
| S-641-68.2 | 17 | 7.31 | 2.46; 2.96; e 3.49 |
| S-300-48.0 | 130 | 7.35 | 3.11 |
| S-700-48.0 | 51 | 7.06 | 2.54; 3.06; e 3.48 |
| S-500-48.0 | 29 | 6.69 | 2.89 ; 2.97; e 3.44 |
| S-500-19.2 | 40 | 7.07 | 2.97 |
| S-500-76.8 | 51 | 6.95 | 3.07 |
| S-500-48.0 (replicate) | 24 | 7.09 | - |
| S-500-48.0 (replicate) | 26 | 6.91 | - |

3.1.1. SEM/EDS

The obtained SEM images indicated that the $\text{TiO}_2/\text{CoFe}_2\text{O}_4$ photocatalysts (Figure 2b) presented a much rougher surface in comparison to the pure cobalt ferrite (Figure 2a), as consequence of the TiO_2 coating. The changes in TIPO/ CoFe_2O_4 mass ratio and calcination temperature during the

synthesis did not significantly affected the appearance of the surfaces of the photocatalysts (Figures S3 and S4). The estimated elementary surface composition, given by the EDS analysis, demonstrated that titanium and oxygen are the most abundant elements on the surface of the catalysts (Figures S5 and S6).

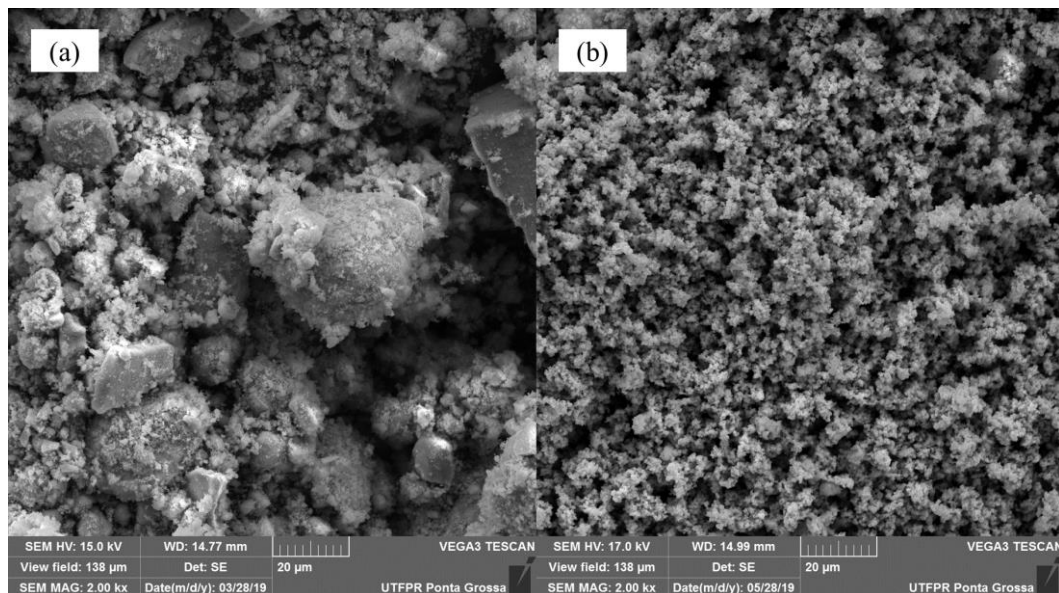


Figure 2 SEM images (1000X) of (a) CoFe₂O₄ and (b) TiO₂/CoFe₂O₄ photocatalyst (S-500-48.0).

3.1.1. Specific surface area and point of zero charge (PZC)

The specific surface area values of TiO₂/CoFe₂O₄ catalysts (Table 3) varied between 14 and 130 m² g⁻¹. Pure ferrite, on the other hand, presented a surface area of 49 m² g⁻¹, indicating that the TiO₂ coating significantly affected the material surface area. The sol-gel process is capable of producing catalysts over a wide range of specific surface area values, which may justify the variation observed in TiO₂/CoFe₂O₄ samples. Lenzi et al. (2011), for example, obtained catalysts throughout the sol-gel process with specific surface areas varying from 17 m² g⁻¹ to 311 m² g⁻¹, depending on the calcination temperature [45]. A strong negative linear relationship (Experimental design, Supplementary Material) between T_{calc} and the surface area was observed for the present samples, so that an increase in the calcination temperature led to a considerable decrease in the specific surface area. This is a consequence of sintering and crystallite growth that occurs at higher temperatures [46]. The TIPO/CoFe₂O₄ mass ratio, in turn, showed a slight positive linear effect and, thus, the use of higher concentrations of titanium isopropoxide during synthesis favored the production of catalysts with a larger surface area, for a given temperature. As previously discussed, SEM images showed that the TiO₂ shell presented a granular and rough aspect (Figure 2), which may be responsible for the increase in the surface area of the catalyst as the TIPO/CoFe₂O₄ mass ratio increased. Besides, an interaction

between factors was observed, since the effect of the TIPO/CoFe₂O₄ mass ratios increase was more pronounced when lower calcination temperature were used (see Table 3, comparison between samples S-359-27.8/ S-359-68.2 and S-641-27.8/S-641-68.2). Likewise, the effect of T_{calc} was more pronounced at higher TIPO concentrations.

In turn, the experimentally obtained point of zero charge values ranged from 6.69 to 7.41 (Table 3 - Specific surface area, point of zero charge (PZC) and band gap values for TiO₂/CoFe₂O₄ catalysts (CCD1)Table 3), with an average value of 7.03. In the literature, slightly different values for the titanium dioxide PZC were reported, such as 6.4 [47], 6.8 [48] and 6.95 for Degussa TiO₂ P-25 [49].

3.1.2. XRD Characterization: diffractograms, crystallite size, and phase distribution

Figure 3 shows the XRD results. The diffractograms of the magnetic material (CoFe₂O₄ –Figure 3a) presented peaks at 2θ values around 30.1°, 35.4°, 37.0°, 43.0°, 53.4°, 56.9° and 62.6°, associated, respectively, with the reflection planes (2 2 0), (3 1 1), (2 2 2), (4 0 0), (4 2 2), (5 1 1) and (4 4 0) of the spinel structure of cobalt ferrite (ICSD 00-022-1086). The observed peaks are similar to those reported by different authors, like Fu et al., for CoFe₂O₄ particles synthesized by co-precipitation and coated with TiO₂ [50], by Houshiar et al., in CoFe₂O₄ samples produced by precipitation, co-precipitation and combustion method [51], and by Ercolino et al. in mixed Fe-Co spinel samples prepared by solution combustion using higher iron contents [52]. In the synthesized TiO₂/CoFe₂O₄ photocatalysts (Figure 3b-j), however, the characteristic peaks of the cobalt ferrite became almost imperceptible, mainly for larger TiO₂ content. Only a reduced signal of the cobalt ferrite peak around 35° remained visible in the diffractograms. This type of response to the TiO₂ coating on magnetic particles was already expected, as previously observed by Fu et al. (2005) in core-shell CoFe₂O₄/TiO₂ particles with higher titanium dioxide contents [50]. The disappearance of the core material peaks may be considered as an indirect proof of the complete coating of the core by the shell material, in core-shell structures [53].

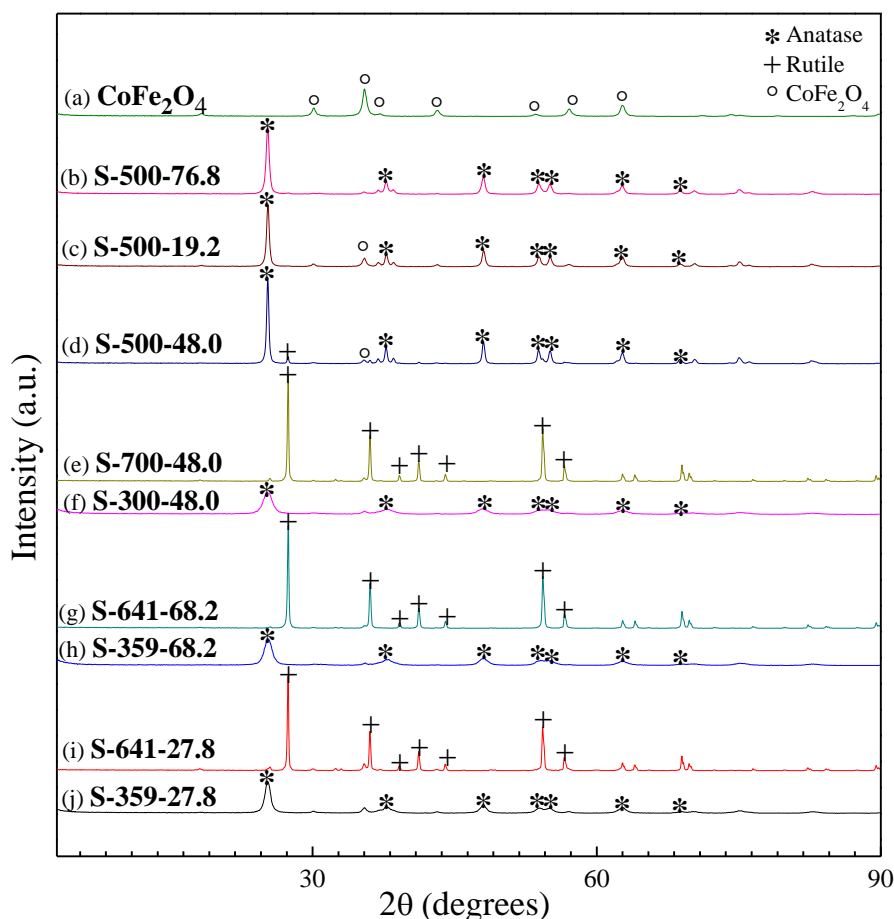


Figure 3 - Diffractograms of (a) cobalt ferrite and (b-j) $\text{TiO}_2/\text{CoFe}_2\text{O}_4$ catalysts produced from solutions with different TIPO/ CoFe_2O_4 mass ratio and calcined at different temperatures.

Regarding TiO_2 phase composition, it have been considerably affected by the calcination temperature. In $\text{CoFe}_2\text{O}_4/\text{TiO}_2$ catalysts calcined at temperatures less than or equal to 500 °C (Figure 3b-d, f, h, and j) TiO_2 was found, predominantly in the anatase form – from 90% to 98% of anatase, according to the Spurr equation (Table 4). In the diffractograms, this phase formation is confirmed by the peaks at 2θ values around 25.4°, 37.7°, 48.0°, 53.8°, 55.0°, 62.6° and 68.6°, corresponding to the (1 0 1), (0 0 4), (2 0 0), (1 0 5), (2 1 1), (2 0 4) and (1 1 6) crystalline planes of anatase (ICSD 01-071-1167). Likewise, similar peaks were observed by Fu et al. (2005) [50], in the diffractograms of $\text{CoFe}_2\text{O}_4/\text{TiO}_2$ nanoparticles calcined at temperatures above 300 °C. The rutile phase of TiO_2 , in turn, was only observed in samples calcined at higher temperatures (Figure 3e, g and i). Thus, the peaks at 27.4°, 36.1°, 39.2°, 41.2°, 44.0°, 54.3° and 56.6° can be indexed, respectively, to the (1 1 0), (1 0 1), (2 0 0), (1 1 1), (2 1 0), (2 1 1) and (2 2 0) crystalline planes of rutile (ICSD 01-076-0318). The elevation of the temperature above 500 °C during the heating treatment caused a considerable increase in the percentage of rutile (Table 3), which was the predominant phase in the photocatalysts calcined at 641 and 700 °C – from 97 to 99% of rutile according to the Spurr Equation. Neris et al. (2018) [54], also

observed the predominant formation of rutile in (Co,Mn)Fe₂O₄@TiO₂ particles calcined at 700 °C. The present results are also in agreement with the experimental results reported by Kandiel et al. (2013) [55] and Singh and Mehata (2019) [56] about the possibility of obtaining rutile from anatase at temperatures equal to or greater than 600 °C.

Table 4 - Anatase and rutile phase percentages calculated using the Spurr and Myers Equation; all phases percentage determined by the Rietveld Refinement; and average crystallite size for CoFe₂O₄, anatase and rutile phases calculated using the Scherrer equation

| SAMPLE | Phase percentage (%) – Spurr and Myers Equation | | Phase Percentage (%) – Rietveld Refinement* | | | | | Crystallite size (nm) | | |
|----------------|---|--------|---|----------------------------------|--------|----------------------------------|--------------------|--|---------------|--------------|
| | Anatase | Rutile | Anatase | CoFe ₂ O ₄ | Rutile | Fe ₂ TiO ₅ | CoTiO ₃ | CoFe ₂ O ₄ (311) | Anatase (101) | Rutile (110) |
| Cobalt ferrite | - | - | - | - | - | - | - | 17.6 | - | - |
| S-359-27.8 | 95 | 5 | 89.0 | 10.5 | 0.5 | - | - | 18.6 | 12.2 | - |
| S-641-27.8 | 3 | 97 | 1.0 | 7.4 | 83.3 | 5.7 | 2.6 | 55.1 | 26.9 | 98.0 |
| S-359-68.2 | 93 | 7 | 91.4 | 7.5 | 1.1 | - | - | 26.2 | 8.8 | - |
| S-641-68.2 | 1 | 99 | 0.1 | 2.9 | 91.6 | 4.1 | 1.4 | 54.3 | 54.9 | 84.6 |
| S-300-48.0 | 91 | 9 | 90.6 | 8.4 | 1.0 | - | - | 22.1 | 7.5 | - |
| S-700-48.0 | 2 | 98 | 0.3 | 2.8 | 90.9 | 4.6 | 1.4 | 58.0 | 49.5 | 95.9 |
| S-500-48.0 | 90 | 10 | 87.4 | 6.1 | 6.5 | - | - | 28.1 | 36.1 | 56.4 |
| S-500-19.2 | 98 | 2 | 83.6 | 15.9 | 0.5 | - | - | 19.7 | 28.2 | - |
| S-500-76.8 | 97 | 3 | 93.8 | 4.7 | 1.4 | - | - | 21.3 | 23.0 | - |

In a more detailed analysis using the Rietveld refinement methodology (Supplementary Material, Figures S7 and S8), it was possible to identify the presence of Fe₂TiO₅ and CoTiO₃ in the catalysts calcined at 641 and 700°C (Table 4). Similarly to the present samples, the formation of mixed oxides between TiO₂ and CoFe₂O₄ was also reported by of Sun et al. (2013) and Li et al. (2012), which obtained, respectively, Fe₂TiO₅ in TiO₂/CoFe₂O₄ photocatalysts [57] and CoTiO₃ and FeTiO₃ in TiO₂/CoFe₂O₄ nanofibers [58]. Ferric pseudobrookite (Fe₂TiO₅) is an iron-titanium oxide with orthorhombic structure (*Cmcm* space group) [59], commonly used as pigments [60]. These pigments are characterized by an intense brown color, with minor yellow and red components [61], so that the presence of Fe₂TiO₅ in samples S-641-27.8, S-641-68.2 and S-700-48.0, even in small amounts (4.1 – 5.7% wt%), resulted in a change in their color in comparison to the other catalysts, which presented more grayish tones (Figure 1a). Sun et al. also obtained the Fe₂TiO₅ phase in TiO₂/CoFe₂O₄ photocatalysts synthesized using cold plasma [57]. According to the authors, the pseudobrookite formation resulted from the diffusion of Fe³⁺ ions of the core material surface into the TiO₂ shell. Such process was favored by the similarity of Fe³⁺ and Ti⁴⁺ radius size and by open channels in the rutile structure [57]. Thus, the Fe₂TiO₅ formation only in the catalysts calcined at higher temperatures (641 and 700°C) was clearly induced by the presence of rutile, which was the dominant phase in the three catalysts (Table 3). In the diffractograms, the pseudobrookite phase formation can be confirmed mainly

by the presence of peaks associated with the reflection planes (2 0 1), (1 0 1) and (2 0 3) presented in Figure. Cobalt titanate (CoTiO_3), in turn presents an ilmenite structure, space group $R\bar{3}-H$, and can also be formed at high temperatures [62,63]. Its formation in the samples can be distinguished by the presence of some of its major peaks in the diffractograms (Figure 4), like (1 0 2) and (1 0 4)[62].

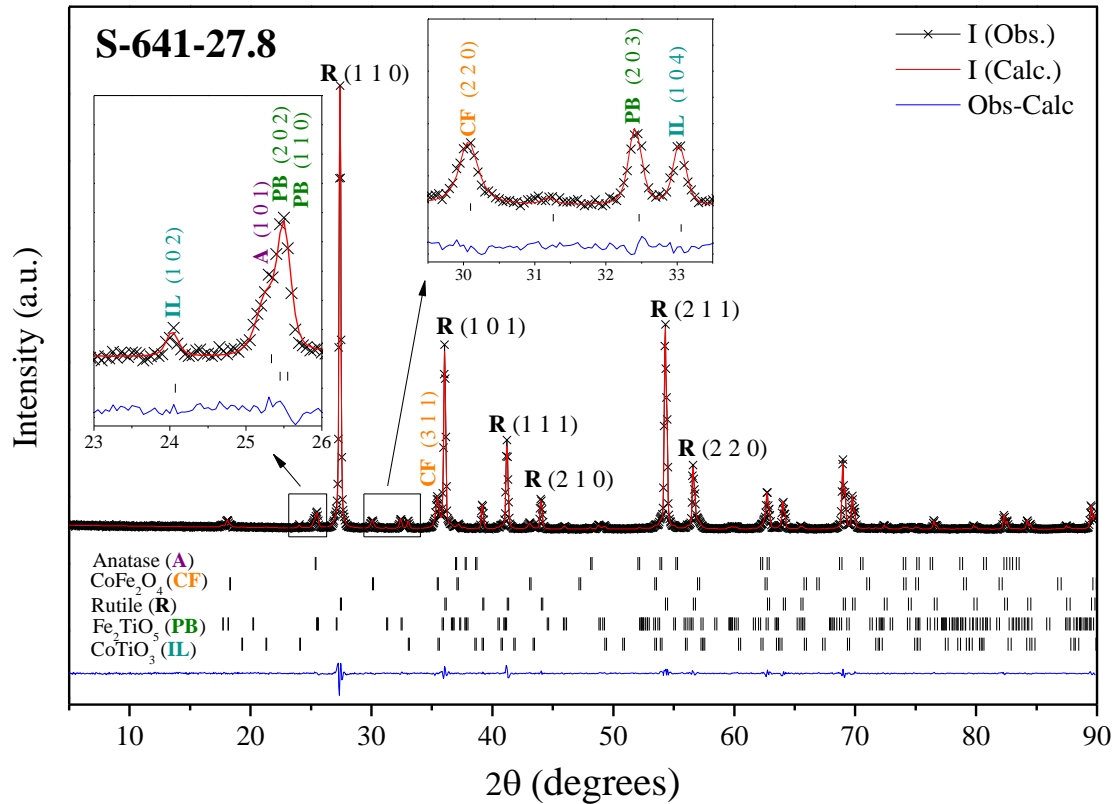


Figure 4 – Rietveld refinement plot of sample S-641-27.8.

The calcination temperature increase also caused a pronounced elevation in the crystallinity of the samples, evidenced by the peaks narrowing in the diffractograms (Figure 3). This is an already well-known phenomenon, previously reported for several materials, including TiO_2 nanoparticles calcined from 200 to 600 °C [48], titania nanotubes heated from 300 to 800 °C [64], TiO_2 thin films photocatalysts calcined up to 900 °C [65], and $\text{TiO}_2/\text{CoFe}_2\text{O}_4$ samples calcined in temperatures from 200 to 450 °C [50]. In the present work, the estimates indicated considerable variations in crystallite size for anatase (from 8.8 nm to 359 °C to 54.9 nm to 641 °C) and rutile (from 56.4 nm to 500 °C to 95.9 to 700 °C). The observed changes, however, were not as pronounced as reported by Neris et al (2018) for $\text{CoMnFe}_2\text{O}_4/\text{TiO}_2$ catalysts, whose crystallite size varied from about 40 nm at 400 °C up to almost 120 nm at 650 °C [54]. Interestingly, rutile phase presented crystallites larger than the coexisting anatase phase crystallites in all samples, which has already been reported in the literature [66].

3.1.3. Photoacoustic spectroscopy

The Photoacoustic Spectroscopy (PAS) results of the photocatalysts are presented in Figure 5. The photoacoustic signal of the samples showed the existence of two distinct groups of samples (Figure 5a and b), with sample S-500-48.0 presenting an intermediate behavior between the two groups. The first group (S-359-27.8, S-359-68.2, S-300-48.0, S-500-19.2 and S-500-76.8) showed a broad absorption band between 225 and 400 nm (Figure 5a), while the second group (S-641-27.8, S-641-68.2 and S-700-48.00) presented a peak around 280 nm and a wide shoulder starting from 325 nm (Figure 5b). The absorption peak at 280 nm possibly corresponds to titanium nanodomains and the another one at about 380 nm is due to a ligand-to-metal charge-transfer transition (LMCT) from O^{2-} to Ti^{4+} [67]. Applying the phase-resolved photoacoustic method (PRPA) [68] in the spectra, it was also possible observed two different absorption peaks between 225-400 nm for the group of samples in Figure 4a, but with a blue shift about 10 nm (270 nm) and 30 nm (350 nm). The region between 400–650 nm is considered to be the intrinsic absorption bands of Fe^{3+} resulting of excitation processes and overlapping the ligand field transition (about 430 nm) [69–71]. The intrinsic absorption bands of the Co^{2+} cation can be centered in close location at 400-550 nm [71]. Samples calcined at higher temperatures (Figure 5b) showed an increase in the absorption band at 430 nm for the Fe^{3+} ions, which suggests a decrease of bound oxygen. Consequently, for these samples, the absorption band at 280 nm also increased, which shows the presence of titanium nanodomains and their growth as a function of temperature, showing an increase in the order of structural organization of the nanodomains, that is, an increase in their size. The presence of these nanodomains can be associated with the existence of specific defects and distortions in the semiconductor oxide network. These results agree with the diffusion of Fe^{3+} ions of the core material surface into the TiO_2 shell and the dominant presence of the rutile phase (Table 4).

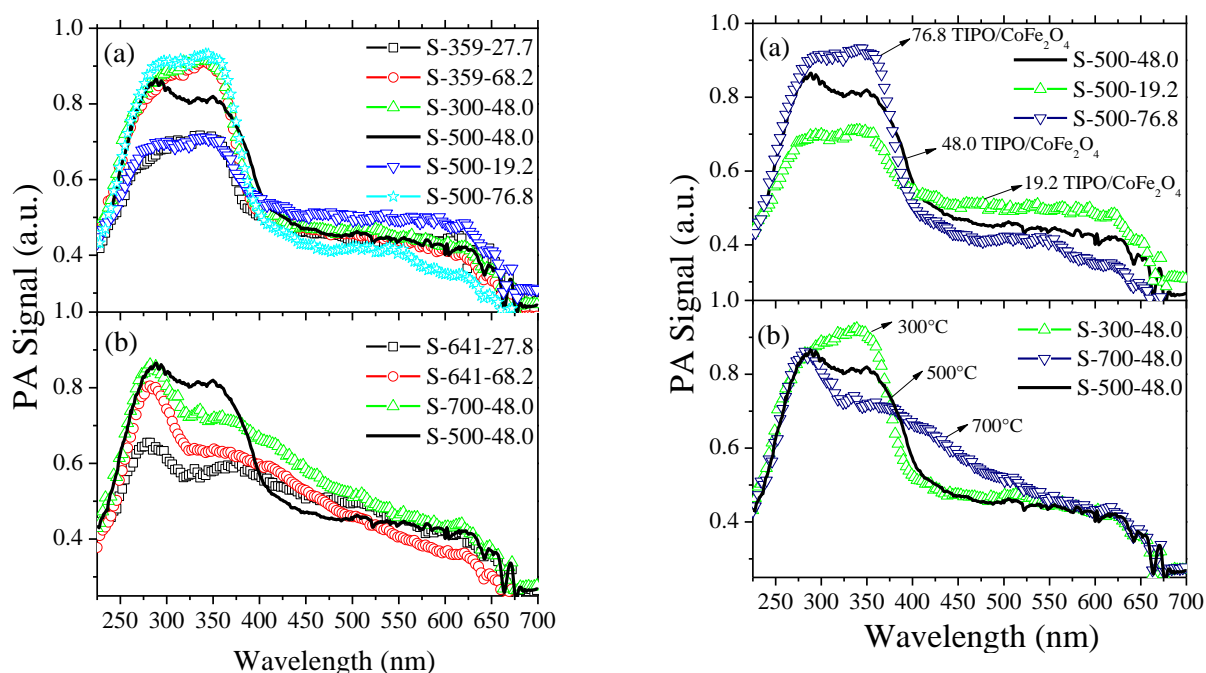


Figure 5 - Comparison of the photoacoustic signals of the photocatalysts. Comparison of the photoacoustic signal of samples (a) calcined at the same temperature (500 °C) and (b) prepared using the same TIPO/CoFe₂O₄ mass ratio (12.5% of TIPO).

The effects of TIPO/CoFe₂O₄ mass ratio and T_{calc} in the photoacoustic signal can be more clearly perceived by observing Figure 5c and Figure 5d, respectively. Analyzing Figure 5c, it can be seen that, for the same calcination temperature, the increase in the TIPO/CoFe₂O₄ mass ratio causes an increase in the absorption band signal attributed to TiO₂ (225-400 nm) and a decrease in the signal from 400 nm referring to cations. This behavior, in Figure 5c, must be due to the increase in the TiO₂ layer. For samples produced with the same TIPO/CoFe₂O₄ mass ratio (Figure 5d), the rise in T_{calc} strongly affects the LMCT from O²⁻ to Ti⁴⁺ and the signal intensity (around 350 nm) becomes lower for higher calcination temperatures. Besides, the increase in the T_{calc} seems to intensify the characteristic Fe³⁺ ions signal at 430 nm. This behavior is possibly mainly related to structural changes caused by the heating of the material, since such catalysts were produced using equal amounts of the titanium dioxide precursor, and, therefore, present very close TiO₂ content values.

The band gap obtained from PAS results (Supplementary Material, Figures S9 and S10) showed two types of behavior (Figure S11). For samples S-359-27.8, S-359-68.2, S-300-48.0, S-500-19.2 and S-500-76.8, it was observed that the signal formed a broader and flatter peak, with a single well-defined band gap value (see, typically, graph S-359-27.8 inserted in Supplementary Material). In addition, these samples presented only the anatase composition phase (Figure 1a). However, for samples S-641-27.8, S-641-68.2 and S-700-48.00, the spectra presented a more defined peak and three band gap values (see, typically, graph S-641-27.8), probably due to the predominance of the rutile

composition phase (Figure 1a) and larger crystallites (Tabela 4). Sample S-359-27.8, on the other hand, presented an intermediate behavior between these two groups (central graph S-359-27.8 inserted in Figure S11). This sample showed a predominance of anatase phase but larger size of crystallite for rutile phase. Therefore, the results obtained suggest that with the increase in the calcination temperature and consequent increase in the crystallinity of the samples (formation of the rutile phase, Figure 2), there was the introduction of electronic levels located in the region between the valence and conduction band. Besides, the samples S-641-27.8, S-641-68.2, S-700-48.00 and S-359-27.8 also showed a "red shift" with increasing calcination temperatures (Figure 5b). It seems that the TiO₂ nanoparticles increased in size with increasing calcination temperatures, which is in agreement with the results of previous crystallite size measurements for rutile (Table 4). Thus, when the size of the nanoparticles increases, the powder surface area (Table 3) reduces proportionally, and less light can be absorbed; therefore the PA intensity is diminished. This well-known effect was not observed for samples with lower levels of calcination temperature.

In the literature, the direct gap values for rutile-TiO₂ and anatase-TiO₂ are described as being 3.0 and 3.2 eV, respectively [72], while CoFe₂O₄ films present 2.3 and 2.7 eV values [73,74]. The band-gap values for the catalyst samples in the present work (Table 3), varied between 2.43-3.49 eV, which is something expected due to the TiO₂/CoFe₂O₄ combination. Only a few samples (S-641-27.8, S-641-68.2, S-700-48.00 and S-359-27.8) showed three band-gap values corresponding to cobalt ferrite, to rutile titanium dioxide and to higher than anatase-TiO₂ band-gap. This may indicate some type of interaction between the materials, producing an effect beyond the simple combination (synergistic combination). Besides, calcination temperature and the presence of the rutile phase in the catalysts seemed to play an important role in this behavior since three of these catalysts were calcined at higher temperatures (641 and 700 °C) and presented rutile as the predominant TiO₂ phase. The blue shift observed at lower calcination temperatures for samples with predominant anatase-TiO₂, see spectra for S-359-27.8, S-359-68.2, S-300-48.0, S-500-19.2 and S-500-76.8 in Figure 4a, changed the anatase-TiO₂ band-gap to longer wavelengths (3.05 eV average).

3.2. Se(IV) removal tests

The Se(IV) removal results (adsorption and photocatalysis) for the 19 performed tests (CCD2) are shown in Table S2. Some of the adsorption removal results are not indicated, as they correspond to negative values, probably caused by small variations in the measurements of samples concentration. It is also important to note that the percentages of removal by photocatalysis refer to the variation in

the concentration of Se(IV) between the point of 0 min of exposure to UV radiation (after 30 min of adsorption in the dark) and the point of 2 min of exposure to UV radiation.

Selenium removal after 2 min of photocatalysis varied over a wide range of values (from 1.1% to 99.1% of Se(IV) removal). At the end of the process, it was possible to notice a slight change in the suspension color, which became light orange. The change in the color of the suspension can be related to the formation of Se^0 deposits on the photocatalyst surface, confirming the photoreduction of Se(IV) [28]. In adsorption or photolysis tests, in turn, no color change was observed.

In a 60 min adsorption test Figure S12a, selenium removal occurred since the first minute after catalyst addition, even without exposure to radiation. This removal in the dark, however, was limited and tended to balance after a certain period of adsorption. Right after the lamp was turned on, there was a considerable increase in the removal of selenium, which reached 90% in just 5 min of exposure to UV radiation (S12a).

This behavior observed in S12a indicates that, despite the occurrence of selenium removal by adsorption, photocatalysis plays a fundamental role, significantly increasing and accelerating the selenium removal. However, to confirm whether this change was not caused by the Se(IV) photolysis process, a test was carried out in the absence of catalyst, using only a solution containing formic acid and $500 \mu\text{g L}^{-1}$ of selenite, with pH adjusted to 3.5. The result (S12b) shows that, during 40 min with the lamp on, the removal did not exceed 8%, confirming the efficiency of the photocatalysis.

3.2.1. Se(IV) photocatalytic removal curves: Effect of calcination temperature (T_{calc} , °C), TIPO/CoFe₂O₄ mass ratio and solution pH.

The kinetic curves of Se(IV) photocatalytic removal demonstrate how T_{calc} (Figure 6a and 6d), TIPO/CoFe₂O₄ mass ratio (Figure 6b and 6e) and pH (Figure 6c and 6f) affect the photocatalytic process over 40 min of exposure to UV radiation. The error bar was calculated from the standard deviation of the replicates of the central point and the Student's t parameter for 95% confidence. The percentage of removal by photocatalysis considers the variation in the concentration of Se(IV) between the end of the adsorption process (30 min of adsorption/0 min of photocatalysis) and a given moment after the lamp is turned on.

As can be seen in the removal curves (Figure 6a), the increase in T_{calc} led to a considerable decrease in the photoreduction efficiency of the catalysts. For catalysts calcined at 300 and 500 °C, a small difference was observed only at the beginning of the tests (Figure 6a), but after 40 min of photocatalysis, there was no significant difference in the efficiency of these two photocatalysts (Figure 6a). On the other hand, the photocatalyst calcined at 700 °C was less efficient even after a longer

irradiation time. The comparison of the removal efficiency after 2 min (Figure 6b) evidences the non-linear decrease of Se(IV) removal as calcination temperature increases. These results can be explained by the higher anatase content present in the photocatalysts calcined at 300 and 500 °C, since this phase is already known for having a good activity in selenium photocatalysis [30], as well as by the considerable decrease in specific surface area as the T_{calc} increases (Table 3). Besides that, higher band-gap values, above 3.4 eV, were observed for catalysts subjected to heat treatment at higher temperatures, which negatively affects the photocatalytic performance, since it implies the need for photons with greater energy to promote the formation of the electron/hole pair. Similarly, in the work of Fuziki et al., the photocatalyst with the higher rutile content presented de lower removal efficiency [75].

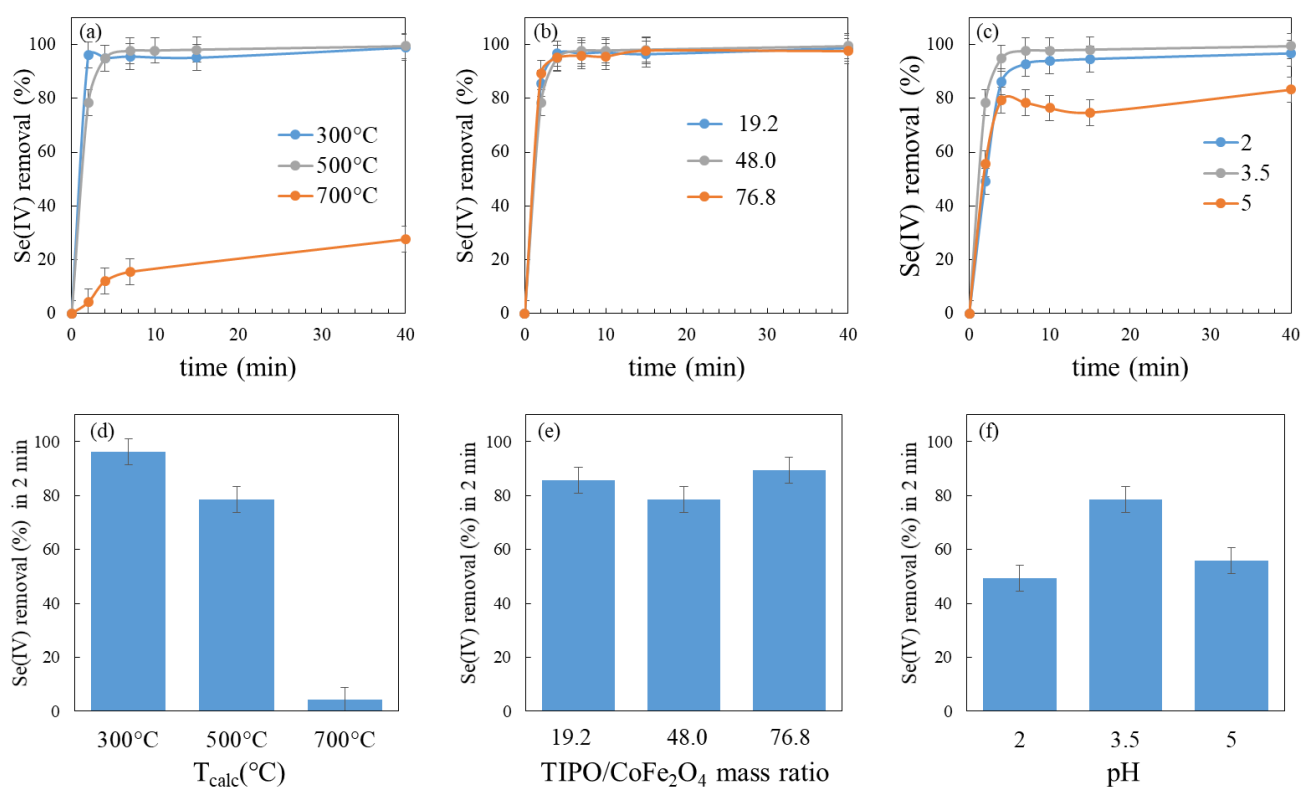


Figure 6 - Se(IV) removal (a-c) over time and (d-f) after 2 min of photocatalysis. (a) and (d) show the effect of calcination temperature for TIPO/CoFe₂O₄ mass ratio = 48.0 and pH = 3.5; (b) and (e) show the effect of TIPO/CoFe₂O₄ mass ratio for T_{calc} = 500 °C and pH = 3.5; (c) and (f) show the effect of pH for TIPO/CoFe₂O₄ mass ratio = 48.0 and T_{calc} = 500 °C;

The variation in the TIPO/CoFe₂O₄ mass ratio used during the synthesis of the photocatalysts did not significantly affect the photoreduction efficiency (Figure 6b). Even when the TIPO/CoFe₂O₄ mass ratio was quadrupled, there were no major changes in the selenium removal curves over time, probably because the change in this synthesis parameter had small impact on the estimated TiO₂

content (between 84 and 95% of TiO_2). A small difference was observed only when the removal after 2 min (figure 6e) was considered, with values varying between 78% and 89%.

The removal curves for different pH values (Figure 6c), in turn, show the great relevance of this factor, which affects not only the selenium reduction kinetics in the initial times, but also changes the maximum removal limit. The results indicated that the removal was higher at pH values closer to 3.5. All pH values tested in the present study were lower than the lowest PZC value (6.69) experimentally determined for the photocatalysts. Thus, the photocatalyst particles presented positively charged surfaces in all the 19 performed tests, favoring the Se(IV) adsorption due to the electrostatic attraction between the surface and selenite ions, which are anions in aqueous medium [25]. However, this phenomenon, by itself, would lead to maximum removal at lower pH values, which does not coincide with the optimal removal observed experimentally at pH between 2 and 5 (Figure 6f). Such behavior would be explained by the competitive adsorption of selenium and formate ions in the photocatalyst surface, as stated by Tan et al. (2003) [28]. According to the mechanism proposed by Nguyen et al. (2005) [13], selenite ions can be reduced to Se(0) both by the direct action of the photogenerated electrons present in the conduction band (CB) of the photocatalyst, or by the reaction between the selenite ions and the formed Se(-2) ions (Figure 7). The first pathway would result in the formation of Se(0) deposits on the surface of the photocatalyst, while the second would lead to the formation of discrete Se(0) particles in the reaction medium [13]. In any case, by either the first or the second route, the adsorption of the Se(IV) ions on the photocatalyst surface is a critical step in selenium reduction.

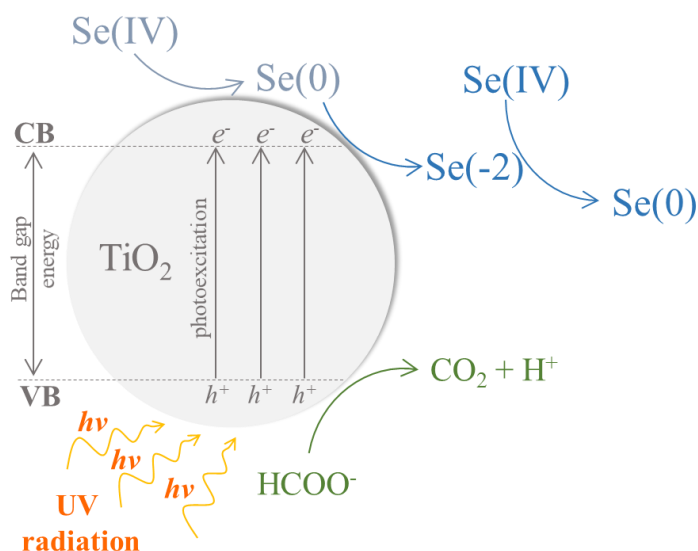


Figure 7 – Se(IV) photocatalytic reduction mechanism

On the other hand, it is also necessary to consider the role played by formic acid as hole scavenger in the process, avoiding the recombination of the electron/hole pair, and also its capacity to

form reducing radicals for selenium reduction [29]. Thus, the selenium removal rate is affected by both the adsorption of selenite and formate ions on the photocatalyst, so that the optimal condition occurs when both ions are adsorbed in an appropriate proportion. It has already been demonstrated experimentally that while selenium anions adsorption is favored at lower pH, formic acid adsorption increases at higher pH values [28]. In their studies on the selenate [Se(VI)] photoreduction, Tan et al. (2003) [28] concluded that the optimal stoichiometric ratio of adsorbed formate:selenate ions would be 3:1 and that such condition would be achieved by varying the concentrations of the reagents (selenium and formic acid) and the pH of the solution. Since in the present work the concentration of Se(IV) and formic acid were kept constant, it follows that the only factor capable of altering this adsorption ratio would be the pH of the solution, justifying the existence of an optimal pH for photocatalysis.

3.2.2. Analysis of the effects and response surface of the Central Composite Designs

The obtained results were also analyzed by using a surface response methodology, in order to evaluate the effects T_{calc} and TIPO/CoFe₂O₄ mass ratio on the photocatalysts' specific surface area, PZC, band gap and anatase content, as well as the effects of pH, T_{calc} and TIPO/CoFe₂O₄ mass ratio on the Se(IV) photocatalytic removal. The obtained response surfaces are presented in Figure 7 and 8, and the effects estimates and ANOVA table for each response are presented in Supplementary Material.

Regarding the validity of the adjusted models, it is important to make some considerations. According to the experimental design analysis, none of the effects was significant for the PZC, considering 95% confidence. This result leads to the conclusion that the two considered factors (T_{calc} and TIPO/CoFe₂O₄ mass ratio), within the range used in the experiments, do not affect the PZC of the photocatalyst. The R^2 value for specific surface area ($R^2=0.95488$, $R^2_{adj}=0.90977$), band gap ($R^2=0.91894$, $R^2_{adj}=0.87384$), anatase content ($R^2=0.91825$, $R^2_{adj}=0.78199$) and photocatalytic removal ($R^2=0.9306$, $R^2_{adj}=0.8611$) models were relatively good, suggesting a considerable agreement of the experimental results with the model. According to the ANOVA table (Supplementary Materials, Tables S4, S6, S8 and S11), in turn, the models adjusted to BET surface area and photocatalytic removal were significant ($p=0.0022<0.05$ and $p=0.0003<0.05$, respectively), but the band gap and anatase content models were not. This may be caused by the fact that the residuals were considered for error estimation of the last two models. Besides that, even the significant models for surface area and photocatalytic removal also presented significant lack of fit ($p=0.026126<0.05$ and $p=0.0045<0.05$). This indicates that the models are not perfectly fitted and do not allow the accurate

estimation of the response, mainly in the regions more distant of the center of the planning. Given the low variation in the central point results for BET area and photocatalytic removal (see Table 3), it is considered that the experimental error was low, so that the lack of fit results from the inadequacy of the second-order model to describe the results (Supplementary Material). This inadequacy was more pronounced for anatase content and photocatalytic removal, whose experimental results were limited by a maximum and minimum possible value (0 and 100%), which could not be represented by a second-order model, which tended to $-\infty$. To a more accurate model, a small region of the planning should be investigated. Despite this, the models can still be used to have an overall view of the main effects of the factors, and the responses surfaces graph can allow the visualization of the general behavior of the responses as it can be seen in Figure 8, by how the surface graph is in agreement with variations of the experimental results (blue points).

The effects estimates (Supplementary Material) indicated that calcination temperature was the most significant factor for all the considered responses. It presented a negative linear effect for photocatalytic removal, specific surface area and anatase content, so that the increase in the calcination temperature of the catalysts led to a decrease in the cited responses. The opposite was observed for band gap response, so that the positive linear effect reflects the increase of the property value as the T_{calc} increases. The decrease/increase of the responses with the temperature, however, was not linear, and a significant positive quadratic effect of temperature was observed in specific surface area and band gap response, as well as a negative quadratic effect in photocatalytic removal case. All these behaviors can be easily visualized in Figure 8a-d.

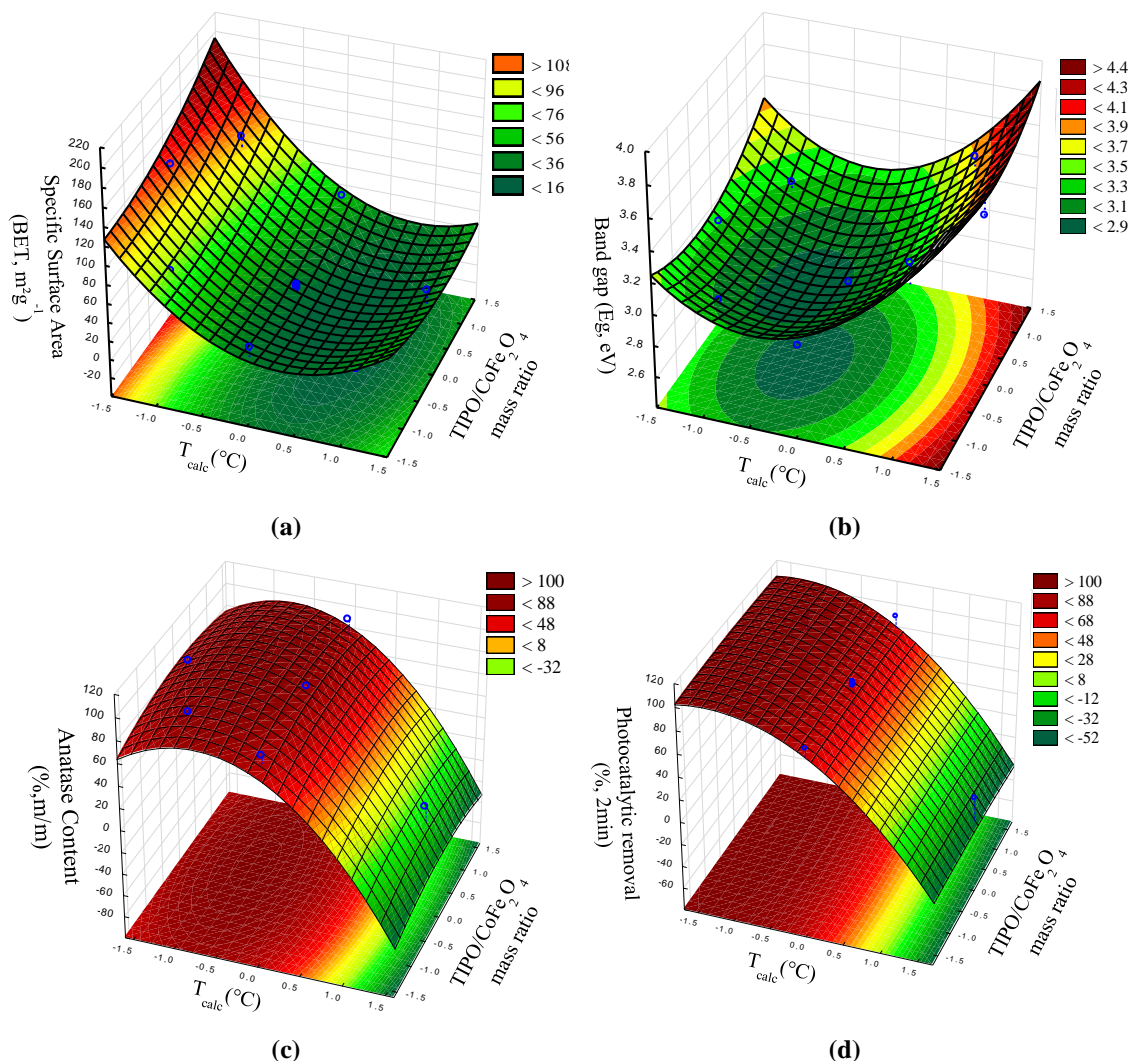


Figure 8 – Response surface plots for (a) BET specific surface area, (b) band gap, (c) anatase content (%) and (d) photocatalytic Se(IV) removal.

Such relevant impact of T_{calc} in the photocatalysts' properties and photocatalytic activity was already expected, since it is well known that the calcination temperature can directly affect the catalyst structure, crystallinity and specific surface area [56]. It is interesting to highlight the similarity between the response surface obtained for anatase content and Se(IV) photocatalytic removal response surface (Figure 8c and 8d). This suggests that the most relevant property of the photocatalyst for the studied process was the anatase content, as the higher removal percentages were obtained using catalysts with higher anatase content (lower calcination temperatures). This leads to the conclusion that Se(IV) reduction is not favorable using rutile phase. In addition to the anatase effect, it is important to say that the photocatalysts with better performance (low T_{calc}) presented also higher BET specific surface areas (Figure 8a) and lower band gap values (Figure 8b).

The TIPO/CoFe₂O₄ mass ratio, within the considered values, did not seem to have considerably affected the studied responses, being significant only for BET surface area (Table S4). The variation in the concentration of TIPO used in the synthesis caused a very small variation of the content of TiO₂ present in the samples (84% to 95%, aprox.), and therefore did not have a great impact on the results. In this sense, it is unnecessary to use high levels of TIPO, representing only an increase in costs for the process.

For the photocatalytic reduction of Se(IV), the only significant factors were the calcination temperature, as previously discussed, and pH. The negative quadratic effect observed for pH confirms the existence of an optimal value for this factor within the studied range (see Figure 9). When these two factors are considered, the optimal condition for the process (red region in Figure 9) is achieved by using catalysts calcined at T_{calc} lower than 500°C and using pH values around 3.5.

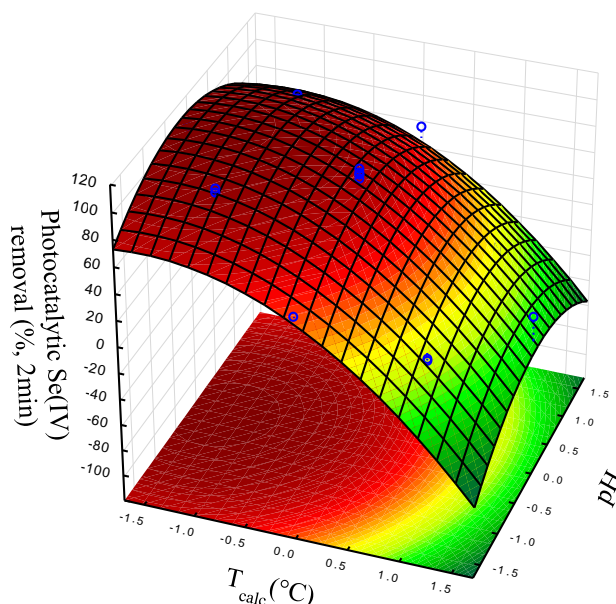


Figure 9 - Response surface plots for photocatalytic Se(IV) removal.

3.2.3. Reuse test and magnetic separation

After five cycles of photocatalysis, the TiO₂/CoFe₂O₄ photocatalyst still had considerable Se(IV) removal capacity (Figure 10a), which indicates the possibility of catalyst reuse. The results showed a small decrease of removal efficiency over the cycles, starting from around 99.0% at the end first cycle, to 98.5%, 98.0%, 95.0% and, finally 96.5% at the end of the fifth cycle. On the other hand, the photocatalyst color considerably changed, from gray in the first test to dark orange/brown at the

end of the fifth test. This color change may be related to the deposition of selenium on the photocatalyst surface [28].

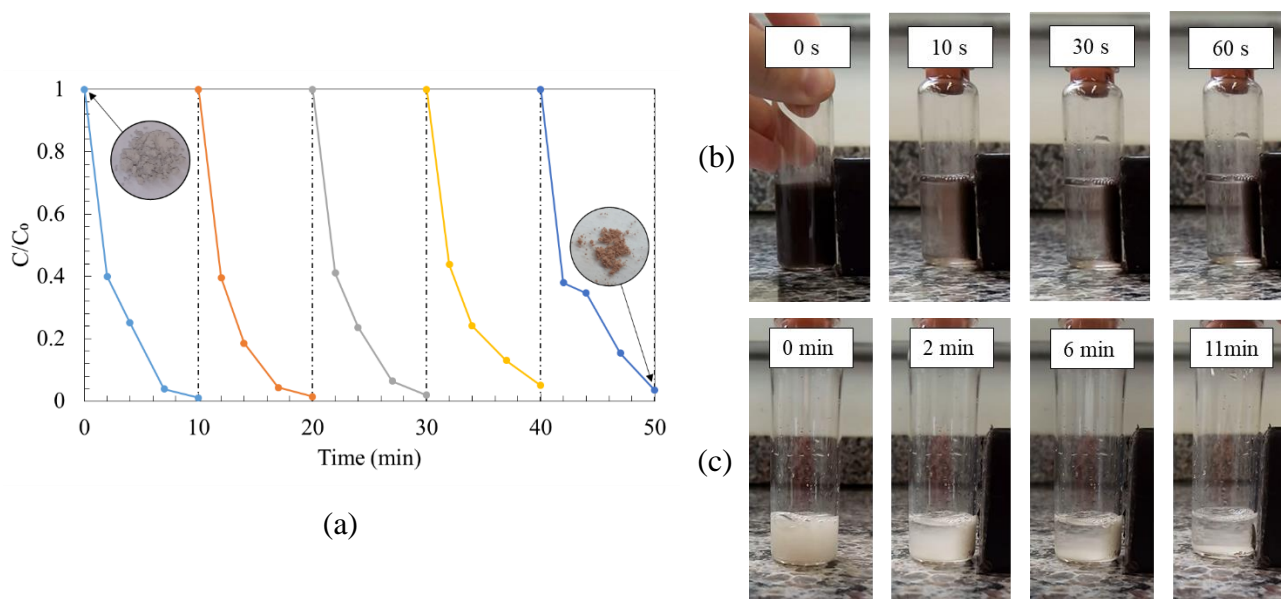


Figure 10 – (a) Se(IV) concentration over five consecutive cycles of photocatalysis; Magnetic separation of (b) CoFe₂O₄ and (c) TiO₂/CoFe₂O₄ particles from water by the action of a neodymium magnet.

Regarding the magnetism of the particles, it was observed that the cobalt ferrite was strongly magnetic and easily separable from the aqueous medium (Figure 10b) with the aid of a neodymium magnet (see Materials and Methods section, for the magnet description). When coated with TiO₂, the particles still retained their magnetic properties, and could even be separated magnetically after the synthesis step. However, due to the titania coating layer, the separation took about eleven times longer (Figure 9c). Such response to the TiO₂ coating was already expected, as reported by Fu et al. (2005), who verified the decrease in coercivity and specific magnetization of the particles with the increase in the percentage of TiO₂ in the sample [50]. Based on what was previously discussed, it is assumed that the titania layer covering the photocatalysts synthesized in the present work was thick, which may have led to a considerable decrease in the magnetic properties of the core-shell catalysts. Reducing the TiO₂ layer can be an interesting alternative to improve the magnetic separation of the catalyst.

4. CONCLUSIONS

It was possible, through different routes of sol-gel synthesis, to produce CoFe₂O₄/TiO₂ photocatalysts. The characterization of the catalysts by XRD proved the formation of the ferrite with spinel structure and the anatase and rutile phases of TiO₂ in quantities that varied according to the calcination temperature. In addition, it was possible to characterize the photocatalysts by different techniques, and

to establish relationships between synthesis parameters and the specific surface area and material band gap.

When applied in the photoreduction of Se(IV), the synthesized catalysts proved to be efficient, achieving removals greater than 99%. The best conditions involved the use of calcined catalysts at lower temperatures (close to 300 °C) and at pH values close to 3.5. Within the percentage range of isopropoxide used and given the employed synthesis conditions, it was not possible to observe a significant effect of this factor on the response.

The coating of cobalt ferrite with TiO₂ affected the magnetic properties of the photocatalysts, however, they were sufficiently preserved to allow their separation by the action of a magnet. In addition, it was shown that the catalysts remained a satisfactory ability to reduce the Se(IV) ion, even after five photocatalytic cycles.

Acknowledgements: The authors wish to thank the Fundação Araucaria, UTFPR, and CNPq for the financial support and C²MMA laboratory and Central de Análises of UTFPR campus Pato Branco for the use of the facilities

5. REFERENCES

- [1] L.C. Tan, Y. V Nancharaiah, E.D. van Hullebusch, P.N.L. Lens, Selenium: environmental significance, pollution, and biological treatment technologies, *Biotechnol. Adv.* 34 (2016) 886–907. <https://doi.org/10.1016/j.biotechadv.2016.05.005>.
- [2] A.D. Lemly, Aquatic selenium pollution is a global environmental safety issue, *Ecotoxicol. Environ. Saf.* 59 (2004) 44–56. [https://doi.org/10.1016/S0147-6513\(03\)00095-2](https://doi.org/10.1016/S0147-6513(03)00095-2).
- [3] K.S. Prabhu, X.G. Lei, Selenium, *Adv. Nutr.* 7 (2016) 415–417. <https://doi.org/10.3945/an.115.010785>.
- [4] A. Torres-Vega, B.F. Pliego-Rivero, G.A. Otero-Ojeda, L.M. Gómez-Oliván, P. Vieyra-Reyes, Limbic system pathologies associated with deficiencies and excesses of the trace elements iron, zinc, copper, and selenium, *Nutr. Rev.* 70 (2012) 679–692. <https://doi.org/10.1111/j.1753-4887.2012.00521.x>.
- [5] S.W. Hwang, H.J. Lee, K.S. Suh, S.T. Kim, S.W. Park, D.Y. Hur, D. Lee, J.K. Seo, H.S. Sung, Changes in murine hair with dietary selenium excess or deficiency, *Exp. Dermatol.* 20 (2011) 367–369. <https://doi.org/10.1111/j.1600-0625.2010.01207.x>.
- [6] J.-C. Zhou, S. Zheng, J. Mo, X. Liang, Y. Xu, H. Zhang, C. Gong, X.-L. Liu, X.G. Lei, Dietary Selenium Deficiency or Excess Reduces Sperm Quality and Testicular mRNA Abundance of Nuclear Glutathione Peroxidase 4 in Rats, *J. Nutr.* 147 (2017) 1947–1953. <https://doi.org/10.3945/jn.117.252544>.
- [7] M. Vinceti, M. Vicentini, L.A. Wise, C. Sacchetti, C. Malagoli, P. Ballotari, T. Filippini, M. Malavolti, P.G. Rossi, Cancer incidence following long-term consumption of drinking water with high inorganic selenium content, *Sci. Total Environ.* 635 (2018) 390–396. <https://doi.org/10.1016/j.scitotenv.2018.04.097>.
- [8] M. Vinceti, F. Bonvicini, K.J. Rothman, L. Vescovi, F. Wang, The relation between amyotrophic lateral sclerosis and inorganic selenium in drinking water: a population-based case-

- control study, *Environ. Heal.* 9 (2010) 77. <https://doi.org/10.1186/1476-069X-9-77>.
- [9] M. Vinceti, P. Ballotari, C. Steinmaus, C. Malagoli, F. Luberto, M. Malavolti, P.G. Rossi, Long-term mortality patterns in a residential cohort exposed to inorganic selenium in drinking water, *Environ. Res.* 150 (2016) 348–356. <https://doi.org/10.1016/j.envres.2016.06.009>.
- [10] A.D. Lemly, Selenium poisoning of fish by coal ash wastewater in Herrington Lake, Kentucky, *Ecotoxicol. Environ. Saf.* 150 (2018) 49–53. <https://doi.org/10.1016/j.ecoenv.2017.12.013>.
- [11] M.A.R. Abdel-Moati, Speciation of selenium in a Nile Delta lagoon and SE Mediterranean Sea mixing zone, *Estuar. Coast. Shelf Sci.* 46 (1998) 621–628. <https://doi.org/10.1006/ecss.1997.0307>.
- [12] F. Séby, M. Potin-Gautier, E. Giffaut, G. Borge, O.F.X. Donard, A critical review of thermodynamic data for selenium species at 25°C, *Chem. Geol.* 171 (2001) 173–194. <https://doi.org/10.1016/S0009-25410000246-1>.
- [13] V.N.H. Nguyen, D. Beydoun, R. Amal, Photocatalytic reduction of selenite and selenate using TiO₂ photocatalyst, *J. Photochem. Photobiol. A Chem.* 171 (2005) 113–120. <https://doi.org/10.1016/j.jphotochem.2004.09.015>.
- [14] Institute of Medicine, Dietary Reference Intakes for Vitamin C, Vitamin E, Selenium, and Carotenoids Panel on Dietary Antioxidants and Related Compounds, Subcommittees on Upper Reference Levels of Nutrients and Interpretation and Uses of DRIs, Standing Committee on the Scientific, 2000. <https://doi.org/10.1080/13664530.2013.813766>.
- [15] Brasil, Ministério da Saúde. Portaria de Consolidação nº 5, de 28 de setembro de 2017. Consolidação das normas sobre as ações e os serviços de saúde do Sistema Único de Saúde, *Diário Of. Da União.* (2017) 360. <https://doi.org/10.1007/s13398-014-0173-7.2>.
- [16] P. Cordoba, L.C. Staicu, Flue gas desulfurization effluents: An unexploited selenium resource, *Fuel.* 223 (2018) 268–276. <https://doi.org/10.1016/j.fuel.2018.03.052>.
- [17] S. HUANG, M. HUA, J. FENG, X. ZHONG, Y. JIN, B. ZHU, H. LU, Assessment of selenium pollution in agricultural soils in the Xuzhou District, Northwest Jiangsu, China, *J. Environ. Sci.* 21 (2009) 481–487. [https://doi.org/10.1016/S1001-0742\(08\)62295-0](https://doi.org/10.1016/S1001-0742(08)62295-0).
- [18] WHO, Guidelines for Drinking- water Quality, 2017.
- [19] Y. He, Y. Xiang, Y. Zhou, Y. Yang, J. Zhang, H. Huang, C. Shang, L. Luo, J. Gao, L. Tang, Selenium contamination, consequences and remediation techniques in water and soils: A review, *Environ. Res.* 164 (2018) 288–301. <https://doi.org/10.1016/j.envres.2018.02.037>.
- [20] N. De la Cruz, J. Giménez, S. Esplugas, D. Grandjean, L.F. de Alencastro, C. Pulgarín, Degradation of 32 emergent contaminants by UV and neutral photo-fenton in domestic wastewater effluent previously treated by activated sludge, *Water Res.* 46 (2012) 1947–1957. <https://doi.org/10.1016/j.watres.2012.01.014>.
- [21] L. V. Bora, R.K. Mewada, Visible/solar light active photocatalysts for organic effluent treatment: Fundamentals, mechanisms and parametric review, *Renew. Sustain. Energy Rev.* 76 (2017) 1393–1421. <https://doi.org/10.1016/j.rser.2017.01.130>.
- [22] C. Byrne, G. Subramanian, S.C. Pillai, Recent advances in photocatalysis for environmental applications, *J. Environ. Chem. Eng.* 6 (2018) 3531–3555. <https://doi.org/10.1016/j.jece.2017.07.080>.
- [23] A. Farrokhi, F. Feizpour, M. Asaadzadeh, Degradation of hazardous organic dyes with solar-driven advanced oxidation process catalyzed by the mixed metal–organic frameworks, *Appl. Organomet. Chem.* (2019) e4928. <https://doi.org/10.1002/aoc.4928>.
- [24] A.G.S. Prado, L.B. Bolzon, C.P. Pedroso, A.O. Moura, L.L. Costa, Nb₂O₅ as efficient and recyclable photocatalyst for indigo carmine degradation, *Appl. Catal. B Environ.* 82 (2008) 219–224. <https://doi.org/10.1016/j.apcatb.2008.01.024>.
- [25] T.T.Y. Tan, M. Zaw, D. Beydoun, R. Amal, The formation of nano-sized selenium-titanium dioxide composite semiconductors by photocatalysis, *J. Nanoparticle Res.* 4 (2002) 541–552. <https://doi.org/10.1023/A:1022858409731>.

- [26] N. Aman, T. Mishra, J. Hait, R.K. Jana, Simultaneous photoreductive removal of copper (II) and selenium (IV) under visible light over spherical binary oxide photocatalyst, *J. Hazard. Mater.* 186 (2011) 360–366. <https://doi.org/10.1016/j.jhazmat.2010.11.001>.
- [27] T.T.. Tan, C.. Yip, D. Beydoun, R. Amal, Effects of nano-Ag particles loading on TiO₂ photocatalytic reduction of selenate ions, *Chem. Eng. J.* 95 (2003) 179–186. [https://doi.org/10.1016/S1385-8947\(03\)00103-7](https://doi.org/10.1016/S1385-8947(03)00103-7).
- [28] T.T.. Tan, D. Beydoun, R. Amal, Photocatalytic reduction of Se(VI) in aqueous solutions in UV/TiO₂ system: importance of optimum ratio of reactants on TiO₂ surface, *J. Mol. Catal. A Chem.* 202 (2003) 73–85. [https://doi.org/10.1016/S1381-1169\(03\)00205-X](https://doi.org/10.1016/S1381-1169(03)00205-X).
- [29] T. Tan, D. Beydoun, R. Amal, Effects of organic hole scavengers on the photocatalytic reduction of selenium anions, *J. Photochem. Photobiol. A Chem.* 159 (2003) 273–280. [https://doi.org/10.1016/S1010-6030\(03\)00171-0](https://doi.org/10.1016/S1010-6030(03)00171-0).
- [30] V.N.H. Nguyen, R. Amal, D. Beydoun, V. Nu Hoai Nguyen, R. Amal, D. Beydoun, Photocatalytic reduction of selenium ions using different TiO₂ photocatalysts, *Chem. Eng. Sci.* 60 (2005) 5759–5769. <https://doi.org/10.1016/j.ces.2005.04.085>.
- [31] A.M. Díez, F.C. Moreira, B.A. Marinho, J.C.A. Espíndola, L.O. Paulista, M.A. Sanromán, M. Pazos, R.A.R. Boaventura, V.J.P. Vilar, A step forward in heterogeneous photocatalysis: Process intensification by using a static mixer as catalyst support, *Chem. Eng. J.* 343 (2018) 597–606. <https://doi.org/10.1016/j.cej.2018.03.041>.
- [32] A.Y. Shan, T.I.M. Ghazi, S.A. Rashid, Immobilisation of titanium dioxide onto supporting materials in heterogeneous photocatalysis: A review, *Appl. Catal. A Gen.* 389 (2010) 1–8. <https://doi.org/10.1016/j.apcata.2010.08.053>.
- [33] T.A. Gad-Allah, S. Kato, S. Satokawa, T. Kojima, Treatment of synthetic dyes wastewater utilizing a magnetically separable photocatalyst (TiO₂/SiO₂/Fe₃O₄): Parametric and kinetic studies, *Desalination*. 244 (2009) 1–11. <https://doi.org/10.1016/j.desal.2008.04.031>.
- [34] A. Madhumitha, V. Preethi, S. Kanmani, Photocatalytic hydrogen production using TiO₂ coated iron-oxide core shell particles, *Int. J. Hydrogen Energy*. 43 (2018) 3946–3956. <https://doi.org/10.1016/j.ijhydene.2017.12.127>.
- [35] S. Khashan, S. Dagher, N. Tit, A. Alazzam, I. Obaidat, Novel method for synthesis of Fe₃O₄@TiO₂ core/shell nanoparticles, *Surf. Coatings Technol.* 322 (2017) 92–98. <https://doi.org/10.1016/j.surfcoat.2017.05.045>.
- [36] V.A. Sakkas, M.A. Islam, C. Stalikas, T.A. Albanis, Photocatalytic degradation using design of experiments: A review and example of the Congo red degradation, *J. Hazard. Mater.* 175 (2010) 33–44. <https://doi.org/10.1016/j.jhazmat.2009.10.050>.
- [37] D.C. Montgomery, *Design and Analysis of Experiments*, 8th ed., John Wiley & Sons, Incorporated, 2012.
- [38] P. Vlazan, M. Stoia, Structural and magnetic properties of CoFe₂O₄ nanopowders, prepared using a modified Pechini method, *Ceram. Int.* 44 (2018) 530–536. <https://doi.org/10.1016/j.ceramint.2017.09.207>.
- [39] Y. Li, X. Xu, D. Qi, C. Deng, P. Yang, X. Zhang, Novel Fe₃O₄@TiO₂ Core–Shell Microspheres for Selective Enrichment of Phosphopeptides in Phosphoproteome Analysis, *J. Proteome Res.* 7 (2008) 2526–2538. <https://doi.org/10.1021/pr700582z>.
- [40] G.C. Bond, *Heterogeneous catalysis: principles and applications*, 2 nd, Clarendon Press-Oxford, New York, 1987.
- [41] W.A. Thompson, C. Perier, M.M. Maroto-Valer, Systematic study of sol-gel parameters on TiO₂ coating for CO₂ photoreduction, *Appl. Catal. B Environ.* 238 (2018) 136–146. <https://doi.org/10.1016/j.apcatb.2018.07.018>.
- [42] R.A. Spurr, H. Myers, Quantitative Analysis of Anatase-Rutile Mixtures with an X-Ray Diffractometer, *Anal. Chem.* 29 (1957) 760–762. <https://doi.org/10.1021/ac60125a006>.
- [43] L.S. Čerović, S.K. Milonjić, M.B. Todorović, M.I. Trtanj, Y.S. Pogozhev, Y. Blagoveschenskii,

- E.A. Levashov, Point of zero charge of different carbides, *Colloids Surfaces A Physicochem. Eng. Asp.* 297 (2007) 1–6. <https://doi.org/10.1016/j.colsurfa.2006.10.012>.
- [44] V.V.D.S. Guillarduci, J.P. De Mesquita, P.B. Martelli, H.D.F. Gorgulho, Adsorção de fenol sobre carvão ativado em meio alcalino, *Quim. Nova.* 29 (2006) 1226–1232. <https://doi.org/10.1590/S0100-40422006000600015>.
- [45] G.G. Lenzi, C.V.B. Fávero, L.M.S. Colpini, H. Bernabe, M.L. Baesso, S. Specchia, O.A.A. Santos, Photocatalytic reduction of Hg(II) on TiO₂ and Ag/TiO₂ prepared by the sol-gel and impregnation methods, *Desalination.* 270 (2011) 241–247. <https://doi.org/10.1016/j.desal.2010.11.051>.
- [46] O. Carp, C.L. Huisman, A. Reller, Photoinduced reactivity of titanium dioxide, *Prog. Solid State Chem.* 32 (2004) 33–177. <https://doi.org/10.1016/j.progsolidstchem.2004.08.001>.
- [47] K.B. Fontana, G.G. Lenzi, E.C.R. Seára, E.S. Chaves, Comparision of photocatalysis and photolysis processes for arsenic oxidation in water, *Ecotoxicol. Environ. Saf.* 151 (2018) 127–131. <https://doi.org/10.1016/j.ecoenv.2018.01.001>.
- [48] D. Dodoo-Arhin, F.P. Buabeng, J.M. Mwabora, P.N. Amaniampong, H. Agbe, E. Nyankson, D.O. Obada, N.Y. Asiedu, The effect of titanium dioxide synthesis technique and its photocatalytic degradation of organic dye pollutants, *Heliyon.* 4 (2018). <https://doi.org/10.1016/j.heliyon.2018.e00681>.
- [49] J. Fernández, J. Kiwi, C. Lizama, J. Freer, J. Baeza, H.D. Mansilla, Factorial experimental design of Orange II photocatalytic discolouration, *J. Photochem. Photobiol. A Chem.* 151 (2002) 213–219. [https://doi.org/10.1016/S1010-6030\(02\)00153-3](https://doi.org/10.1016/S1010-6030(02)00153-3).
- [50] W. Fu, H. Yang, M. Li, M. Li, N. Yang, G. Zou, Anatase TiO₂ nanolayer coating on cobalt ferrite nanoparticles for magnetic photocatalyst, *Mater. Lett.* 59 (2005) 3530–3534. <https://doi.org/10.1016/j.matlet.2005.06.071>.
- [51] M. Houshiar, F. Zebhi, Z.J. Razi, A. Alidoust, Z. Askari, Synthesis of cobalt ferrite (CoFe₂O₄) nanoparticles using combustion, coprecipitation, and precipitation methods: A comparison study of size, structural, and magnetic properties, *J. Magn. Mater.* 371 (2014) 43–48. <https://doi.org/10.1016/j.jmmm.2014.06.059>.
- [52] G. Ercolino, P. Stelmachowski, A. Kotarba, S. Specchia, Reactivity of Mixed Iron–Cobalt Spinels in the Lean Methane Combustion, *Top. Catal.* 60 (2017) 1370–1379. <https://doi.org/10.1007/s11244-017-0826-9>.
- [53] R. Ghosh Chaudhuri, S. Paria, Core/Shell Nanoparticles: Classes, Properties, Synthesis Mechanisms, Characterization, and Applications, *Chem. Rev.* 112 (2012) 2373–2433. <https://doi.org/10.1021/cr100449n>.
- [54] A.M. Neris, W.H. Schreiner, C. Salvador, U.C. Silva, C. Chesman, E. Longo, I.M.G. Santos, Photocatalytic evaluation of the magnetic core@shell system (Co,Mn)Fe₂O₄@TiO₂ obtained by the modified Pechini method, *Mater. Sci. Eng. B.* 229 (2018) 218–226. <https://doi.org/10.1016/j.mseb.2017.12.029>.
- [55] T.A. Kandiel, L. Robben, A. Alkaim, D. Bahnemann, Brookite versus anatase TiO₂ photocatalysts: phase transformations and photocatalytic activities, *Photochem. Photobiol. Sci.* 12 (2013) 602–609. <https://doi.org/10.1039/C2PP25217A>.
- [56] M.K. Singh, M.S. Mehata, Phase-dependent optical and photocatalytic performance of synthesized titanium dioxide (TiO₂) nanoparticles, *Optik (Stuttg.)* 193 (2019) 163011. <https://doi.org/10.1016/j.ijleo.2019.163011>.
- [57] D. Sun, Y. Han, S. Gao, X. Zhang, Surface modification of titania-coated cobalt ferrite magnetic photocatalyst by cold plasma, *Surf. Coatings Technol.* 228 (2013) S516–S519. <https://doi.org/10.1016/j.surfcoat.2012.04.072>.
- [58] C.J. Li, J.N. Wang, B. Wang, J.R. Gong, Z. Lin, A novel magnetically separable TiO₂/CoFe₂O₄ nanofiber with high photocatalytic activity under UV-vis light, *Mater. Res. Bull.* 47 (2012) 333–337. <https://doi.org/10.1016/j.materresbull.2011.11.012>.

- [59] W.Q. Guo, S. Malus, D.H. Ryan, Z. Altounian, Crystal structure and cation distributions in the FeTi₂O₅-Fe₂TiO₅ solid solution series, *J. Phys. Condens. Matter.* 11 (1999) 6337–6346. <https://doi.org/10.1088/0953-8984/11/33/304>.
- [60] J. Maloney, Titanate Pigments: Colored Rutile, Priderite, and Pseudobrookite Structured Pigments, in: *High Perform. Pigment.*, Wiley-VCH Verlag GmbH & Co. KGaA, Weinheim, Germany, 2009: pp. 53–73. <https://doi.org/10.1002/9783527626915.ch6>.
- [61] M. Dondi, F. Matteucci, G. Cruciani, G. Gasparotto, D.M. Tobaldi, Pseudobrookite ceramic pigments: Crystal structural, optical and technological properties, *Solid State Sci.* 9 (2007) 362–369. <https://doi.org/10.1016/j.solidstatesciences.2007.03.001>.
- [62] T. Acharya, R.N.P. Choudhary, Structural, dielectric and impedance characteristics of CoTiO₃, *Mater. Chem. Phys.* 177 (2016) 131–139. <https://doi.org/10.1016/j.matchemphys.2016.04.005>.
- [63] Y.J. Lin, Y.H. Chang, W.D. Yang, B.S. Tsai, Synthesis and characterization of ilmenite NiTiO₃ and CoTiO₃ prepared by a modified Pechini method, *J. Non. Cryst. Solids.* 352 (2006) 789–794. <https://doi.org/10.1016/j.jnoncrysol.2006.02.001>.
- [64] J. Yu, B. Wang, Effect of calcination temperature on morphology and photoelectrochemical properties of anodized titanium dioxide nanotube arrays, *Appl. Catal. B Environ.* 94 (2010) 295–302. <https://doi.org/10.1016/j.apcatb.2009.12.003>.
- [65] J.-G. Yu, H.-G. Yu, B. Cheng, X.-J. Zhao, J.C. Yu, W.-K. Ho, The Effect of Calcination Temperature on the Surface Microstructure and Photocatalytic Activity of TiO₂ Thin Films Prepared by Liquid Phase Deposition, (2003). <https://doi.org/10.1021/jp036158y>.
- [66] A.A. Gribb, J.F. Banfield, Particle size effects on transformation kinetics and phase stability in nanocrystalline {TiO₂}, *Am. Miner.* 82 (1997) 717–728. <https://www.degruyter.com/downloadpdf/j/ammin.1997.82.issue-7-8/am-1997-7-809/am-1997-7-809.pdf> (accessed September 30, 2018).
- [67] A. Aronne, M. Fantauzzi, C. Imparato, D. Atzei, L. De Stefano, G. D’Errico, F. Sannino, I. Rea, D. Pirozzi, B. Elsener, P. Pernice, A. Rossi, Electronic properties of TiO₂-based materials characterized by high Ti³⁺ self-doping and low recombination rate of electron–hole pairs, *RSC Adv.* 7 (2017) 2373–2381. <https://doi.org/10.1039/C6RA27111A>.
- [68] A. Novatski, A. Somer, F.G. Maranha, E.C.F. de Souza, A.V.C. Andrade, S.R.M. Antunes, C.P.F. Borges, D.T. Dias, A.N. Medina, N.G.C. Astrath, Effect of magnetic coupling on non-radiative relaxation time of Fe³⁺ sites on LaAl_{1-x}Fe_xO₃ pigments, *J. Appl. Phys.* 123 (2018) 075101. <https://doi.org/10.1063/1.4998642>.
- [69] B. Hannoyer, M. Lenglet, J. Dürr, R. Cortes, Spectroscopic evidence of octahedral iron (III) in soda-lime silicate glasses, *J. Non. Cryst. Solids.* 151 (1992) 209–216. [https://doi.org/10.1016/0022-3093\(92\)90031-E](https://doi.org/10.1016/0022-3093(92)90031-E).
- [70] D.M. Sherman, N. Vergo, Optical (diffuse reflectance) and Mossbauer spectroscopic study of nontronite and related Fe-bearing smectites, *Am. Mineral.* 73 (1988) 1346–1354.
- [71] L. Kernazhitsky, V. Shymanovska, T. Gavrilko, V. Naumov, V. Kshnyakin, T. Khalyavka, A comparative study of optical absorption and photocatalytic properties of nanocrystalline single-phase anatase and rutile TiO₂ doped with transition metal cations, *J. Solid State Chem.* 198 (2013) 511–519. <https://doi.org/10.1016/j.jssc.2012.11.015>.
- [72] A. Kudo, Y. Miseki, Heterogeneous photocatalyst materials for water splitting, *Chem. Soc. Rev.* 38 (2009) 253–278. <https://doi.org/10.1039/B800489G>.
- [73] K.K. Kefeni, B.B. Mamba, T.A.M. Msagati, Application of spinel ferrite nanoparticles in water and wastewater treatment: A review, *Sep. Purif. Technol.* 188 (2017) 399–422. <https://doi.org/10.1016/j.seppur.2017.07.015>.
- [74] B.S. Holinsworth, D. Mazumdar, H. Sims, Q.-C. Sun, M.K. Yurtisigi, S.K. Sarker, A. Gupta, W.H. Butler, J.L. Musfeldt, Chemical tuning of the optical band gap in spinel ferrites: CoFe₂O₄ vs NiFe₂O₄, *Appl. Phys. Lett.* 103 (2013) 082406. <https://doi.org/10.1063/1.4818315>.
- [75] M.E.K. Fuziki, E. Abreu, A.E. De Carvalho, L.H.B.O. Silva, M.Z. Fidelis, A.M. Tusset, R. Brackmann, D.T. Dias, G.G. Lenzi, Sol-gel Fe/TiO₂ Magnetic Catalysts Applied to Selenium Photoreduction, *Top. Catal.* (2020). <http://doi.org/10.1007/s11244-020-01276-1>